

The high-energy environment of the heavy sub-Earth GJ 367 b indicates likely complete evaporation of its atmosphere

K. Poppenhaeger^{1,2}, L. Ketzer^{1,2}, N. Ilic^{1,2}, E. Magaudda³, J. Robrade⁴, B. Stelzer³, J.H.M.M. Schmitt⁴, and P.C. Schneider⁴

¹ Leibniz Institute for Astrophysics Potsdam (AIP), An der Sternwarte 16, 14482 Potsdam, Germany

² Institute for Physics and Astronomy, University of Potsdam, Karl-Liebknecht-Str. 24/25, 14476 Potsdam-Golm, Germany

³ Institut für Astronomie und Astrophysik (IAAT), Eberhard Karls Universität Tübingen, Sand 1, 72076 Tübingen, Germany

⁴ Hamburger Sternwarte, Gojenbergsweg 112, 21029 Hamburg, Germany

Accepted XXX. Received YYY; in original form ZZZ

ABSTRACT

The planet GJ 367 b is a recently discovered high-density sub-Earth orbiting an M dwarf star. Its composition was modelled to be predominantly iron with a potential remainder of a hydrogen-helium envelope. Here we report an X-ray detection of this planet's host star for the first time, using data from the spectro-imaging X-ray telescope eROSITA onboard the Spectrum-Roentgen-Gamma (SRG) mission. We characterise the magnetic activity of the host star from the X-ray data and estimate the present-day mass-loss rate of the potential atmosphere of the planet driven by the high-energy irradiation. We find that despite the very low activity level of the host star the potential mass loss rate is so high that any atmospheric remainders would evaporate in about 15 million years. Since the activity level of the host star indicates that the system is several Gigayears old, it is very unlikely that the planet currently still hosts any atmosphere.

Key words. planets and satellites: atmospheres – stars: planetary systems – stars: low-mass – stars: coronae – X-rays: individual: GJ 367

1. Introduction

As exoplanet detection techniques have matured, planets in the Earth-sized regime have become detectable. Especially M dwarfs as host stars provide an advantage for the detection of small planets, since their small stellar radii yield sufficiently deep transits when a small rocky planet crosses the star. The planetary radius from transit observations can be combined with the planetary mass from radial velocity measurements to yield the planetary mean density, which in turn allows some inferences on the planetary composition.

Exoplanets which have radii similar to or smaller than Earth have been inferred to have a range of different compositions, with Trappist-1e (Grimm et al. 2018) and *f* (Agol et al. 2021) having similar densities to Earth and Venus, while other exoplanets have been found to display significantly lower densities indicative of water envelopes (for example, Kepler-138b, Jontof-Hutter et al. (2015); Trappist-1h, Agol et al. (2021)). Recently, the small exoplanet GJ 367b was discovered to have a surprisingly high density implying a high iron content (Lam et al. 2021). Modelling by the same authors showed that the planet can be described well if the planet is composed of iron for 90 % of its interior, the remaining outer 10 % consisting of a mantle layer and a small fraction of water ice VII (a specific crystalline form of ice) as well as hydrogen and helium in gaseous form.

Exoplanets have been found to undergo significant atmospheric evolution; one signpost of this is the so-called radius gap of small planets, an observed dearth of planets with radii around $2R_{\oplus}$ (Fulton et al. 2017; Van Eylen et al. 2018). This is typically

interpreted as planets losing their primordial hydrogen-helium envelopes through some process, where bare rocky planets live below the gap and the ones with significant hydrogen-helium envelopes remaining populate the parameter space above the gap. Different processes may be driving this atmospheric mass loss; two prominent scenarios are atmospheric escape driven by the internal heat of the planet (core-driven escape, Gupta & Schlichting 2020), and escape driven by the high-energy irradiation by the host star (see for example Murray-Clay et al. 2009; Owen & Wu 2017; Kubryshkina et al. 2018; Mordasini 2020), which can have a variety of different flavours depending on the assumptions made in the respective models.

Here we report on a first-time X-ray detection of GJ 367b's host star, which is an early M dwarf in the solar neighbourhood (see Table 1 for an overview of the system's properties). The detection was achieved using data from the eROSITA X-ray instrument (section 2). This allows us to determine the coronal properties of the host star (section 3) and to characterize the high-energy environment and possible evaporation rate of the exoplanet associated with irradiation (section 4).

2. Observations and data analysis

eROSITA (Predehl et al. 2021) is an X-ray instrument onboard the Spectrum-Roentgen-Gamma spacecraft (Sunyaev et al. 2021). It was launched in July 2019 into an orbit around the L_2 Lagrange point of the Sun-Earth system. eROSITA consists of seven Wolter telescopes with one camera assembly each and is sensitive to photon energies between 0.2 and 10 keV. eROSITA started an all-sky survey in December 2019, where it scanned

* E-mail: kpoppenhaeger@aip.de

Table 1. Properties of the GJ 367 star-planet system from Lam et al. (2021).

Property	Value
<i>stellar parameters:</i>	
spectral type	M1.0V
mass	$0.454 M_{\odot}$
radius	$0.457 R_{\odot}$
distance	9.41 pc
rotation period	48 ± 2 d
<i>planetary parameters:</i>	
mass	$0.55 M_{\oplus}$
radius	$0.72 R_{\oplus}$
semi-major axis	0.0071 AU
orbital period	0.322 d

the whole sky every six months in great circles roughly perpendicular to the ecliptic. Any point on the sky is scanned every four hours for several eROSITA slews, with the number of slews when a given target is in the field of view depending on the ecliptic latitude of the target.

eROSITA has completed four all-sky surveys to date (named eRASS1 to eRASS4). We accessed the data around GJ 367's position in the form of photon event files for each of the four surveys, and additionally used the source catalogs produced by the consortium. Specifically, we used the stacked source catalog in the current data reduction version from October 31 2022, as released to the eROSITA-DE consortium¹. For the photon event files we used the data processing version 020 of eROSITA-DE. The eROSITA source catalog was constructed by performing a source detection on the stacked X-ray images from the first four eRASS surveys in the 0.2-2.3 keV band, and then using the identified source positions to perform forced photometry in narrower energy bands; this stacked catalog is referred to as eRASS:4. For an overview of the data reduction software for eROSITA see Brunner et al. (2022), and for an overview of the data release of the eRASS1 data see the paper by (Merloni et al. 2024).

We performed a separation-based cross-match of the eRASS:4 catalog to the optical position of GJ 367 as identified in the *Gaia* DR3 catalog (Gaia Collaboration et al. 2022). GJ 367 has a significant proper motion of about 0.7 arcsec per year, and it was observed by eROSITA about half-yearly from June 2020 to December 2021. Therefore we chose the star's position at the epoch of March 31 2021 as its representative mean position for the relevant eROSITA scanning period, yielding coordinates of R.A. = 09:44:28.897 and Decl. = -45:46:47.808. We cross-matched this optical position of GJ 367 with the eRASS:4 catalog and found an X-ray source within an on-sky separation of 6'', which is within two sigma of the typical positional uncertainty of eROSITA; we therefore identify this X-ray source with GJ 367. The effective exposure time at GJ 367's position is about 600 s. Since eROSITA surveys scan the sky on great-circles, the effective exposure time of a sky location varies slightly for different photon energies due to energy-dependent vignetting effects, but this variation is small for the soft X-ray energies at which GJ 367 emits.

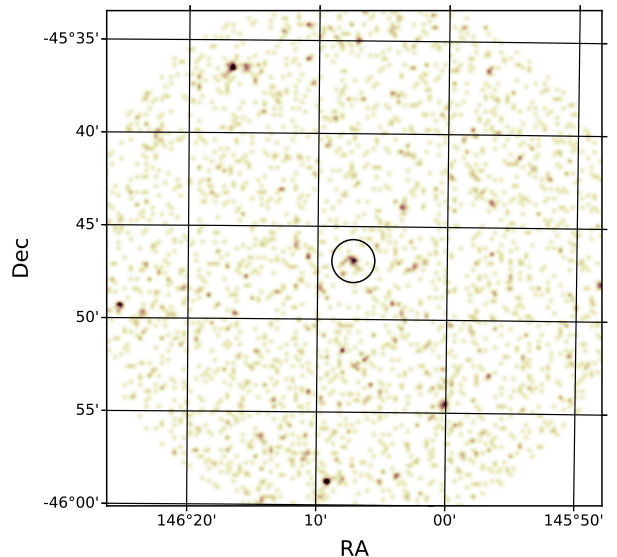


Fig. 1. Combined X-ray image from the first four eRASS surveys around the position of GJ 367, indicated by the circle, in the soft eROSITA X-ray band (0.2 keV to 2.3 keV). GJ 367 displays a clear excess in X-ray photons compared to the ambient background.

3. Results

3.1. X-ray upper limits from previous observations

In the past the position of the GJ 367 system was observed by the ROSAT All-Sky Survey (Boller et al. 2016) and multiple times with the XMM-Newton Slew Survey (Saxton et al. 2008; Freund et al. 2018), both of which yielded unrestrictive upper limits to the X-ray flux of the star. We calculated the corresponding upper limits with the XMM Upper Limit Server² to be $F_{X, \text{ROSAT}} \leq 2.79 \times 10^{-13} \text{ erg s}^{-1} \text{ cm}^{-2}$ from ROSAT and the strictest of the XMM Slew Survey upper limits to be $F_{X, \text{XMM slew}} \leq 6.33 \times 10^{-13} \text{ erg s}^{-1} \text{ cm}^{-2}$. With a stellar distance of 9.41 pc this corresponds to an upper limit to the X-ray luminosity of the star of $L_{X, \text{ROSAT}} \leq 3.0 \times 10^{27} \text{ erg s}^{-1}$.

3.2. X-ray properties from eROSITA

The combined signal from the four completed eRASS scans of GJ 367's position clearly displays an X-ray excess; we show the combined soft X-ray image produced from the photon event files in the 0.2-2.3 keV energy band in Fig. 1.

In the eRASS:4 source catalog, the source we identified with GJ 367 is significantly detected. The detection significance is determined in the eROSITA data reduction as the negative logarithm of the probability that the observed excess counts have arisen as a chance fluctuation of the background, meaning that larger log-likelihood values correspond to more significant source detections. A minimum log-likelihood threshold of 5 was applied in the construction of the catalog; GJ 367 has a log-likelihood value of 32 for the 0.2-2.3 keV energy band, making it a solid detection.

¹ The consortium-internal catalog file name that was used was `all_s4_SourceCat1B_221031_poscorr_mpe_photom.fits`.

² <http://xmmluls.esac.esa.int/upperlimitserver/>

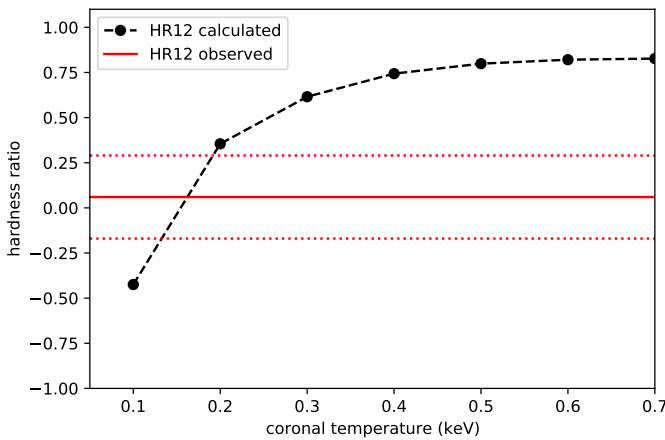


Fig. 2. Measured X-ray hardness ratio HR_{12} of GJ 367 (red solid line, with red dotted lines indicating 1σ uncertainties) compared to the same hardness ratio for simulated X-ray spectra of different coronal temperatures (black dots and dashed line). GJ 367's hardness ratio implies a mean coronal temperature in the 0.13–0.19 keV range, i.e. about 1.5–2.2 million K.

3.2.1. Stellar coronal temperature

The ROSAT non-detection of GJ 367 implies that it has a moderate to low X-ray luminosity for an M dwarf, which we discuss in more detail in section 4.1. The star can therefore be expected to have a soft X-ray spectrum, as X-ray luminosity and temperature are correlated for stellar coronal spectra (see for example Schmitt 1997; Johnstone & Güdel 2015; Magaude et al. 2022).

Since the determination of X-ray fluxes and luminosity depends on the underlying spectral shape, we proceed by estimating the coronal temperature for GJ 367 from the collected eROSITA data.

A total of 24.9 source counts above the background were collected in the 0.2–2.3 keV band; this is a maximum-likelihood estimate for the source counts which takes into account vignetting and is therefore not an integer number. This number of collected counts is small and allows only a low signal-to-noise (S/N) spectrum to be extracted. We therefore first consider the hardness ratio of the two softest bands of the star, with $HR_{12} = (R_2 - R_1)/(R_2 + R_1)$ where R_2 is the excess count rate in the harder band and R_1 in the softer band, and energy bands of 0.2–0.5 and 0.5–1.0 keV are chosen. The hardness ratio from the catalog is listed in Table 2 as well, with $HR_{12} = 0.06 \pm 0.23$.

To convert this into an estimate for the typical coronal temperature of GJ 367, we use the same methodology as used in other works (Poppenhäger et al. 2009; Foster et al. 2022), i.e. simulating coronal spectra over the instrumental spectral response and calculating the resulting hardness ratios as a function of coronal temperature. We show the hardness ratios for the relevant spectral bands derived from the simulated spectra in Fig. 2, together with the measured hardness ratios for GJ 367. We find that the observed hardness ratios are in agreement with a coronal temperature in the range of 0.16 ± 0.03 keV, corresponding to about 1.82 ± 0.34 MK. We point out here the same caveat already mentioned by Foster et al. (2022), that the relationship between the hardness ratio and the coronal temperature is well-defined for stellar coronae with a single dominant temperature component, but may not represent coronae well in which two or more disparate strong temperature components are present.

Table 2. Coronal X-ray fluxes of GJ 367 in the combined first four eRASS scans for several energy bands.

energy band	X-ray flux with 1σ uncertainty ($\text{erg s}^{-1} \text{cm}^{-2}$)	hardness ratio with 1σ uncertainty
<i>narrow eROSITA bands:</i>		
0.2–0.5 keV	$(2.64 \pm 0.88) \times 10^{-14}$	$HR_{12} = 0.06 \pm 0.23$
0.5–1.0 keV	$(1.57 \pm 0.53) \times 10^{-14}$	–
1.0–2.0 keV	$< 0.17 \times 10^{-14}$	–
<i>broad eROSITA soft band:</i>		
0.2–2.3 keV	$(4.71 \pm 1.08) \times 10^{-14}$	–

3.2.2. Stellar X-ray luminosity

The eROSITA source catalogs derive source fluxes from count rates by assuming an underlying absorbed power-law spectrum. In contrast, X-ray emission from stellar coronae is described by an optically thin thermal plasma instead of a power law, which yields different conversion factors between count rates and X-ray fluxes.

Following the procedure from Foster et al. (2022), we determine correction factors to convert the power-law fluxes from the eROSITA catalog into fluxes for an underlying coronal spectrum with a temperature of 1.82 MK. This procedure is described in more detail in Tubín et al. (2024); in short, one simulates an absorbed power-law spectrum and the appropriate coronal spectrum over the eROSITA instrumental response and effective area and calculates the ratio of the two resulting flux conversion factors. For GJ 367, we find that the correction factors are as follows for several energy bands: $F_{\text{cor}, 0.2-2.3 \text{ keV}} = 1.22 F_{\text{pow}, 0.2-2.3 \text{ keV}}$, $F_{\text{cor}, 0.2-0.5 \text{ keV}} = 1.38 F_{\text{pow}, 0.2-0.5 \text{ keV}}$, $F_{\text{cor}, 0.5-1 \text{ keV}} = 1.07 F_{\text{pow}, 0.5-1 \text{ keV}}$, $F_{\text{cor}, 1-2 \text{ keV}} = 0.86 F_{\text{pow}, 1-2 \text{ keV}}$, with F_{cor} being the flux for an underlying coronal spectrum with the derived temperature of 1.82 MK, and F_{pow} being the eROSITA catalog flux using an underlying absorbed power-law spectrum as specified in Brunner et al. (2022). Applying these correction factors yields stellar X-ray fluxes for GJ 367 as listed in Table 2. Unsurprisingly for such a cool corona, the emission is very soft, and within narrow energy bands, the source is only individually detected in the 0.2–0.5 keV and 0.5–1.0 keV band. The 1.0–2.0 keV band shows a weak excess, yielding no significant detection in that band alone. The standard eROSITA energy band of 0.2–2.3 keV yields a total coronal flux, using the correction factor for that band, of $(4.71 \pm 1.08) \times 10^{-14} \text{ erg s}^{-1} \text{cm}^{-2}$. We use this value for the following luminosity and surface flux calculation of GJ 367.

We derive an X-ray luminosity of $(5.0 \pm 1.1) \times 10^{26} \text{ erg s}^{-1}$ in the 0.2–2.3 keV energy band, using the stellar distance of 9.41 pc as listed in Table 1. The detected X-ray luminosity of the host star is, therefore, fainter than the previous ROSAT upper limit by a factor of about six.

Other relevant properties that can be calculated from the stellar X-ray luminosity are the stellar activity indicator $R_X = \log(L_X/L_{\text{bol}})$ and the X-ray flux through the stellar photospheric surface $F_{X, \text{surf}} = L_X/(4\pi R_*^2)$. We estimated the stellar bolometric luminosity from the color relations given by Mann et al. (2015, 2016), which yielded $L_{\text{bol}} = 0.030 L_{\text{bol}, \odot} = 1.1 \times 10^{32} \text{ erg s}^{-1}$. The activity indicator then works out to $R_X = -5.34^{+0.09}_{-0.11}$ and the flux through the stellar surface to $F_{X, \text{surf}} = (3.9 \pm 0.9) \times 10^4 \text{ erg s}^{-1} \text{cm}^{-2}$. We list all relevant X-ray quantities together in Table 3.

Table 3. Derived X-ray properties of the exoplanet host star GJ 367

X-ray property (0.2-2.3 keV band)	Value
X-ray luminosity L_X	$(5.0 \pm 1.1) \times 10^{26} \text{ erg s}^{-1}$
mean coronal temperature T_{cor}	$1.82 \pm 0.34 \text{ MK}$
activity indicator $R_X = \log(L_X/L_{\text{bol}})$	$-5.34^{+0.09}_{-0.11}$
X-ray flux through stellar surface $F_{X, \text{surf}}$	$(3.9 \pm 0.9) \times 10^4 \text{ erg s}^{-1} \text{ cm}^{-2}$
X-ray flux at planetary orbit $F_{X, \text{pl}}$	$3.5 \times 10^3 \text{ erg s}^{-1} \text{ cm}^{-2}$

3.2.3. X-ray variability

GJ 367 does not display any strong variability in the data collected by eRASS1:4 surveys. We show the detected mean count rates per eRASS survey in the right panel of Fig. 3. They display mild variability within a factor of two, but this is consistent with a constant source flux within the uncertainties of the measurements.

4. Discussion

4.1. The present-day magnetic activity environment of GJ 367 b

The derived X-ray properties of GJ 367 mark it as an M dwarf with very low activity. In the context of older surveys of M dwarf X-ray luminosities, such as the sample collected by Schmitt et al. (1995) with ROSAT, it does not seem to be remarkably low in X-ray luminosity. However, this is due to the fact that GJ 367 sits at the high end of the mass and radius range of M dwarfs. The X-ray luminosity is therefore not the most suitable activity indicator to compare the star to other M dwarfs; rather, the fractional X-ray luminosity $R_X = \log(L_X/L_{\text{bol}})$ is of interest, which normalizes for the large size and effective temperature range present in M dwarfs of different masses. This is demonstrated by more recently analyzed X-ray samples of M dwarfs (Magaudda et al. 2022; Caramazza et al. 2023), where GJ 367 does actually sit at the lower end of observed fractional X-ray luminosities with respect to the M dwarfs that occupy a similar mass range to GJ 367.

The fractional X-ray luminosity R_X can be put into context with the stellar rotation period. We calculated GJ 367's Rossby number $Ro = P_{\text{rot}}/\tau_{\text{conv}}$ using the rotation period P_{rot} from Lam et al. (2021) and estimated the convective turnover time τ_{conv} from the relation with $V - K$ color determined by Wright et al. (2018). We derived the fractional X-ray luminosity $R_X = -5.34$ in section 3.2.2. We compare this to the sample presented by Magaudda et al. (2022), highlighting the M dwarfs with masses between 0.4 and $0.6 M_{\odot}$ in turquoise (see Fig. 4). Here we see that GJ 367 falls into the slowly-rotating, low-activity tail of the distribution. It is among the lowest-activity M dwarfs with measured rotation periods, but not an outlier in terms of the overall rotation-activity relation. Together with its long rotation period (see Table 1), the low X-ray activity suggests a mature main-sequence age of the star of several Gyr (see for example Gruner et al. 2023; Curtis et al. 2020).

While the stellar coronal temperature and absolute X-ray luminosity are on the low end compared to other M dwarfs, the high-energy environment of the exoplanet GJ 367 b is intense nevertheless, since the planet is located at a distance of only 0.0071 AU to the host star. We calculate the high-energy flux the planet receives in its orbit from the planetary orbital parameters derived by Lam et al. (2021), which are also listed in Table 1. We find an X-ray flux at the planetary orbit of $F_{X, \text{pl}} = 3.5 \times 10^3 \text{ erg s}^{-1} \text{ cm}^{-2}$ in the 0.2-2.3 keV band. This is lower by only about a factor of two than the X-ray irradiation

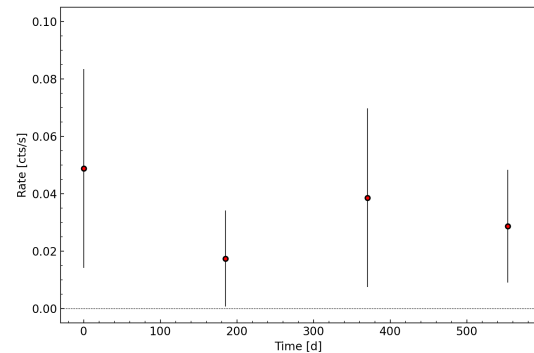


Fig. 3. X-ray light curve of GJ 367 over the four half-yearly eRASS surveys, displayed as source count rates in the 0.2-2.3 keV band with 1σ uncertainties.

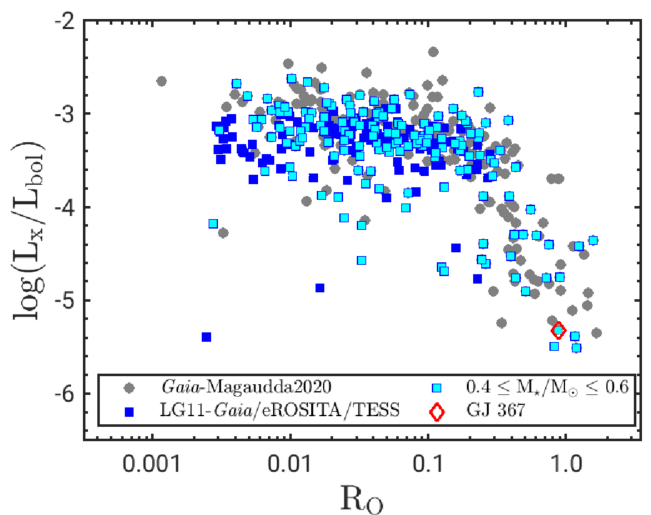


Fig. 4. GJ 367's X-ray activity in the context of other M dwarfs in the same mass range (from Magaudda et al. 2022) as a function of the Rossby number. GJ 367 falls into the low-activity tail of the distribution and is one of the lowest-activity M dwarfs with detected X-ray emission and rotation period; however, it is not unusually X-ray inactive compared to other M dwarfs at large Rossby numbers.

of the evaporating hot Jupiter HD 189733 b (Poppenhaeger et al. 2013; Pillitteri et al. 2014).

4.2. Stellar activity effects on any remaining atmosphere of the planet

Modelling of the planet GJ 367 b suggests a core consisting predominantly of iron surrounded by a mantle, with the possibility of a thin hydrogen-helium atmosphere on top (Lam et al. 2021). Assuming there is indeed a thin, gaseous atmosphere left that can be lost due to photoevaporation driven by the high-energy emission of the host star, we estimate the present-day mass loss rate of the planet. While the X-ray luminosity is known thanks to eROSITA, the extreme-UV (EUV) emission of the host star needs to be estimated, since no observatories are currently operating in the EUV regime. EUV photons are an important contributor to the photoionization of hydrogen, which in turn can cause heating and mass loss from the planetary atmosphere (e.g. Watson et al. 1981; Murray-Clay et al. 2009).

We use two empirical scaling relationships to obtain a general estimate of the EUV flux. One of them calculates the EUV flux based on an X-ray and EUV surface flux scaling relation (Johnstone et al. 2021), while the other scales X-ray and EUV energy bands for late-type stars based on synthetic XUV spectra (Sanz-Forcada et al. 2011). Both use an input X-ray band of 0.1-2.4 keV and calculate EUV fluxes for a band of 0.013 to 0.1 keV (equalling 100 to 920 Å). We estimate GJ 367's X-ray luminosity in the 0.1-2.4 keV band to be 5.7×10^{26} erg s $^{-1}$, using its measured luminosity in the 0.2-2.3 keV band and coronal temperature of 1.82 MK in the WebPIMMS tool³. We then obtain $L_{\text{EUV}} = 2.8 \times 10^{27}$ erg s $^{-1}$ and $L_{\text{EUV}} = 6.4 \times 10^{27}$ erg s $^{-1}$ for the surface flux and synthetic spectra relations, respectively. This leads to a combined X-ray and EUV (XUV) luminosity of $L_{\text{XUV}} = 3.3 \times 10^{27}$ erg s $^{-1}$ for the surface flux relation, and $L_{\text{XUV}} = 7.0 \times 10^{27}$ erg s $^{-1}$ for the synthetic spectra relation. For GJ 367, the EUV flux is relatively well constrained, with both estimates agreeing within a factor of two. We do not make use of the Linsky et al. (2014) X-ray to Ly α relation due to its applicability to K-F spectral types, only.

With an estimate of the present-day XUV emission of the host star in hand, we calculate the energy-limited mass loss rate of GJ 367 b as follows (see e.g. Owen & Jackson 2012; Lopez et al. 2012):

$$\dot{M}_{\text{en-lim}} = -\epsilon \frac{(\pi R_{\text{XUV}}^2) F_{\text{XUV}}}{KGM_{\text{pl}}/R_{\text{pl}}} = -\epsilon \frac{3\beta^2 F_{\text{XUV}}}{4GK\rho_{\text{pl}}}. \quad (1)$$

M_{pl} and ρ_{pl} are the mass and density of the planet, R_{pl} and R_{XUV} the planetary radii at optical and XUV wavelengths; $\beta = R_{\text{XUV}}/R_{\text{pl}}$ is used as a shorthand in the following. The high-energy XUV flux received by the planet is given by F_{XUV} , and the efficiency of the atmospheric escape by ϵ . In the energy-limited regime, the heating efficiency of stellar XUV radiation is predicted to be on the order of 10 to 30 % (see e.g. Owen & Wu 2013; Salz et al. 2016) for low mass planets. For our calculation, we choose a conservative constant ϵ of 10 %. Impacts of Roche lobe overflow (Erkaev et al. 2007) are encompassed in the factor K , which can take on values of 1 for no Roche lobe influence and < 1 for planets filling significant fractions of their Roche lobes.

To estimate the effective XUV absorption cross-section, β , we use a scaling relation for the planetary XUV radius as a function of the planetary gravitational potential (Φ_{G}) and the XUV irradiation (Eq. 4 from Salz et al. (2016)). Since GJ 367 b, with $\log_{10}(\Phi_{\text{G}})(\text{erg g}^{-1}) = 11.7$, falls just short the range of applicability of the Salz-relation ($\log_{10}(\Phi_{\text{G}})(\text{erg g}^{-1}) > 12$), we decide to extrapolate just beyond the lower applicability limit to obtain a β of 2.3. If we were to use the lower applicability limit of $\log_{10}(\Phi_{\text{G}})(\text{erg g}^{-1}) = 12$, we would obtain an only slightly lower β of 2.0.

Taking into account the spread in the predicted EUV flux that the planet receives, we obtain present-day mass loss rates between 3.8×10^{10} and 8.2×10^{10} g s $^{-1}$ for the Johnstone et al. (2021) and Sanz-Forcada et al. (2011) EUV relations, respectively. We do not predict the mass-loss rates according to the hydro-based approximation by Kubyshkina et al. (2018), which would in principle be expected to be more realistic than an energy-limited estimate, because their calculations only extend to planets with masses as low as $1 M_{\oplus}$.

³ <https://heasarc.gsfc.nasa.gov/cgi-bin/Tools/w3pimms/w3pimms.pl>

This estimated mass loss rate is moderately high in the context of exoplanets that have been observed to be actively evaporating. For example, the hot Neptune GJ 436 b has been observed to have a giant evaporating hydrogen tail (Kulow et al. 2014; Ehrenreich et al. 2015), with a modelled mass loss rate of about a factor of 10 lower than what we estimate for GJ 367 b. In the past of the system the X-ray and EUV irradiation is expected to have been stronger due to the higher activity of cool stars at younger ages, and therefore its mass loss might have been much higher then. Specific estimates of the total atmospheric mass lost can depend sensitively on the specific spin-down behaviour of the host star (see for example Ketzer & Poppenhaeger 2022; Ketzer et al. 2024), particularly in the case of small planets, and we therefore do not attempt to estimate the mass loss of GJ 367 b at earlier ages of the star-planet system.

However, we can infer the present-day and near-future state of GJ 367 b's potential atmosphere. Since the mass budget for the potentially remaining atmosphere of GJ 367 b is very small with $\lesssim 1\%$ of the planetary mass (Lam et al. 2021), our estimated current evaporation rate would cause the planet's envelope to be fully evaporated quickly. Assuming an average present-day mass loss rate of $\dot{M} = 6.0 \times 10^{10}$ g s $^{-1}$, a potentially remaining hydrogen atmosphere of 1% of the total mass of the planet would be lost within the next ~ 15 Myr.

As we have discussed above, the X-ray luminosity and spectral hardness of the host star suggest that the system is several Gigayears old, in line with the long rotation period derived by Lam et al. (2021). Therefore, it is statistically very unlikely that the planet currently still hosts an atmosphere, when its density can also be modelled by an atmosphere-free iron-dominated rock. This is a purely probabilistic argument: if a remaining atmosphere can evaporate in only 15 Myr during any part of the several Gigayear-long main-sequence phase of the star, it is more likely that it has already evaporated than that we are lucky enough to see this planet in the 15 Myr where its atmosphere might still be present. Nevertheless, small rocky planets like GJ 367 b are interesting laboratories to improve our understanding of atmosphere survival. The specific case of this exoplanet shows that even low-activity M dwarfs can drive significant mass loss rates in the most compact systems.

5. Conclusions

We have presented the first X-ray detection of GJ 367, an M dwarf star hosting a recently discovered, extremely dense mini-Earth. We characterize the host star to have a low-temperature corona and an X-ray luminosity typical for old, inactive M dwarfs in the solar neighborhood. Due to its proximity to the host star, the irradiation of the planet can support evaporation of any potentially remaining gaseous atmosphere. Modelling of GJ 367 b by Lam et al. (2021) has suggested that the planet mainly consists of iron, and the possible existence of a thin gaseous hydrogen-helium atmosphere has not been excluded so far. Here we find that the survival time of the potential atmosphere is very short with about 15 Myr, despite the very low activity level of the host star, making it statistically unlikely that this planet currently hosts any remainders of a gaseous hydrogen-helium atmosphere. Given that this M dwarf's activity level is extremely low and therefore presents a comparatively mild evaporative environment, it can be expected that hydrogen-helium atmospheres are difficult to retain by small, short-orbit planets around M dwarfs in general.

Acknowledgements

KP, NI, and LK acknowledge support from the German Leibniz-Gemeinschaft under project number P67/2018. EM is supported by Deutsche Forschungsgemeinschaft under grant STE 1068/8-1. JR acknowledges support from the DLR under grant 50QR2105 and PCS from DLR grant 50OR2102.

This work is based on data from eROSITA, the soft X-ray instrument aboard SRG, a joint Russian-German science mission supported by the Russian Space Agency (Roskosmos), in the interests of the Russian Academy of Sciences represented by its Space Research Institute (IKI), and the Deutsches Zentrum für Luft- und Raumfahrt (DLR). The SRG spacecraft was built by Lavochkin Association (NPOL) and its subcontractors, and is operated by NPOL with support from the Max Planck Institute for Extraterrestrial Physics (MPE). The development and construction of the eROSITA X-ray instrument was led by MPE, with contributions from the Dr. Karl Remeis Observatory Bamberg & ECAP (FAU Erlangen-Nuernberg), the University of Hamburg Observatory, the Leibniz Institute for Astrophysics Potsdam (AIP), and the Institute for Astronomy and Astrophysics of the University of Tübingen, with the support of DLR and the Max Planck Society. The Argelander Institute for Astronomy of the University of Bonn and the Ludwig Maximilians Universität Munich also participated in the science preparation for eROSITA.

References

Agol, E., Dorn, C., Grimm, S. L., et al. 2021, *PSJ*, 2, 1

Boller, T., Freyberg, M. J., Trümper, J., et al. 2016, *A&A*, 588, A103

Brunner, H., Liu, T., Lamer, G., et al. 2022, *A&A*, 661, A1

Caramazza, M., Stelzer, B., Magaizza, E., et al. 2023, *A&A*, 676, A14

Curtis, J. L., Agüeros, M. A., Matt, S. P., et al. 2020, *ApJ*, 904, 140

Ehrenreich, D., Bourrier, V., Wheatley, P. J., et al. 2015, *Nature*, 522, 459

Erkaev, N. V., Kulikov, Y. N., Lammer, H., et al. 2007, *A&A*, 472, 329

Foster, G., Poppenhaeger, K., Ilic, N., & Schwope, A. 2022, *A&A*, 661, A23

Freund, S., Robrade, J., Schneider, P. C., & Schmitt, J. H. M. M. 2018, *A&A*, 614, A125

Fulton, B. J., Petigura, E. A., Howard, A. W., et al. 2017, *AJ*, 154, 109

Gaia Collaboration, Vallenari, A., Brown, A. G. A., et al. 2022, arXiv e-prints, arXiv:2208.00211

Grimm, S. L., Demory, B.-O., Gillon, M., et al. 2018, *A&A*, 613, A68

Gruner, D., Barnes, S. A., & Weingrill, J. 2023, *A&A*, 672, A159

Gupta, A. & Schlichting, H. E. 2020, *MNRAS*, 493, 792

Johnstone, C. P., Bartel, M., & Güdel, M. 2021, *A&A*, 649, A96

Johnstone, C. P. & Güdel, M. 2015, *A&A*, 578, A129

Jontof-Hutter, D., Rowe, J. F., Lissauer, J. J., Fabrycky, D. C., & Ford, E. B. 2015, *Nature*, 522, 321

Ketzer, L. & Poppenhaeger, K. 2022, *Astronomische Nachrichten*, 343, e10105

Ketzer, L., Poppenhaeger, K., Baratella, M., & Ilin, E. 2024, *MNRAS*, 527, 374

Kubyshkina, D., Fossati, L., Erkaev, N. V., et al. 2018, *ApJ*, 866, L18

Kulow, J. R., France, K., Linsky, J., & Loyd, R. O. P. 2014, *ApJ*, 786, 132

Lam, K. W. F., Csizmadia, S., Astudillo-Defru, N., et al. 2021, *Science*, 374, 1271

Linsky, J. L., France, K., & Ayres, T. 2014, in *Formation, Detection, and Characterization of Extrasolar Habitable Planets*, ed. N. Haghighipour, Vol. 293, 309–314

Lopez, E. D., Fortney, J. J., & Miller, N. 2012, *ApJ*, 761, 59

Magaizza, E., Stelzer, B., Raetz, S., et al. 2022, *A&A*, 661, A29

Mann, A. W., Feiden, G. A., Gaidos, E., Boyajian, T., & von Braun, K. 2015, *ApJ*, 804, 64

Mann, A. W., Feiden, G. A., Gaidos, E., Boyajian, T., & von Braun, K. 2016, *ApJ*, 819, 87

Merloni, A., Lamer, G., Liu, T., et al. 2024, *A&A*, 682, A34

Mordasini, C. 2020, *A&A*, 638, A52

Murray-Clay, R. A., Chiang, E. I., & Murray, N. 2009, *ApJ*, 693, 23

Owen, J. E. & Jackson, A. P. 2012, *MNRAS*, 425, 2931

Owen, J. E. & Wu, Y. 2013, *ApJ*, 775, 105

Owen, J. E. & Wu, Y. 2017, *ApJ*, 847, 29

Pillitteri, I., Wolk, S. J., Lopez-Santiago, J., et al. 2014, *ApJ*, 785, 145+

Poppenhaeger, K., Schmitt, J. H. M. M., & Wolk, S. J. 2013, *ApJ*, 773, 62

Poppenhaeger, K., Robrade, J., Schmitt, J. H. M. M., & Hall, J. C. 2009, *A&A*, 508, 1417

Predehl, P., Andritschke, R., Arefiev, V., et al. 2021, *A&A*, 647, A1

Salz, M., Schneider, P. C., Czesla, S., & Schmitt, J. H. M. M. 2016, *A&A*, 585, L2

Sanz-Forcada, J., Micela, G., Ribas, I., et al. 2011, *A&A*, 532, A6+

Saxton, R. D., Read, A. M., Esquej, P., et al. 2008, *A&A*, 480, 611

Schmitt, J. H. M. M. 1997, *A&A*, 318, 215

Schmitt, J. H. M. M., Fleming, T. A., & Giampapa, M. S. 1995, *ApJ*, 450, 392

Sunyaev, R., Arefiev, V., Babyshkin, V., et al. 2021, *A&A*, 656, A132

Tubin, D., Krumpe, M., Lamer, G., et al. 2024, *A&A*, accepted by *A&A*

Van Eylen, V., Agentoft, C., Lundkvist, M. S., et al. 2018, *MNRAS*, 479, 4786

Watson, A. J., Donahue, T. M., & Walker, J. C. G. 1981, *Icarus*, 48, 150

Wright, N. J., Newton, E. R., Williams, P. K. G., Drake, J. J., & Yadav, R. K. 2018, *MNRAS*, 479, 2351